

Multifunctional Full-Space Metahologram Employing a Monolayer Phase-Encoding Metasurface

Lei Zhu,^{1,*} Wen Juan Zhou,¹ Liang Dong,¹ Qun Wu,² Shah Nawaz Burokur,^{3,†} and Xumin Ding^{4,‡}

¹*Communication and Electronics Engineering Institute, Qiqihar University, Qiqihar 161006, China*

²*Department of Microwave Engineering, Harbin Institute of Technology, Harbin 150001, China*

³*LEME, UPL, Université Paris Nanterre, F92410 Ville d'Avray, France*

⁴*Advanced Microscopy and Instrumentation Research Center, School of Instrumentation Science and Engineering, Harbin Institute of Technology, Harbin 150080, China*



(Received 20 June 2022; revised 15 September 2022; accepted 11 October 2022; published 23 November 2022)

Full-space metasurfaces exhibit considerable capacities in the fields of electromagnetic wave-front tailoring due to their functional and spatial integration, and extensive applications in modern communication systems. However, almost all metasurfaces for wave-front tailoring are implemented by multilayer dielectric cascade structures, which not only present imperfections in the cost and manufacturing process, but are also detrimental to integration. As such, it is highly desirable to actualize a high-performance metasurface that merely relies on elaborated designs and simple manufacturing process. This study combines frequency multiplexing, spatial channel multiplexing, and polarization multiplexing to propose a full-space metahologram with four different information channels based on a thin double-face copper-cladded metasurface. Exploiting the propagation phase, linear-polarized incident waves can be independently manipulated for the reflection semispace. Integrating the Pancharatnam-Berry (PB) phase, circular-polarized incident waves are tailored for the transmission semispace. To validate the concept, a metahologram sample is fabricated and tested. The experimental results are fully consistent with theoretical calculations and numerical simulation results. The metasurface has a useful role in multifunctional metadevices, and paves the way for potential applications in the fields of antennas and communication systems.

DOI: 10.1103/PhysRevApplied.18.054080

I. INTRODUCTION

Since its invention by Denis Gabor in 1948, holography has become the most promising technique to perfectly reconstruct three-dimensional images of objects [1]. The emergence of metasurface presents a platform to code holograms at the subwavelength scale [2]. Metasurfaces are expected to pave the way for high-quality spatial light modulators and a number of metasurfaces have been investigated as holographic devices [3]. Holographic technology paves the way for near-field electromagnetic (EM) wave signal transmission and other related applications, such as industrial detection and sensing, wireless energy transmission, and radio-frequency identification (RFID) systems. Moreover, the proposed holography concept provides a scheme that can achieve accurate and elaborate control of EM near fields, which can offer significant advantages for

short-range communication, detection, security, data storage, and information processing [4]. Tracing back to the generalized Snell's law, anomalous refraction and reflection of electromagnetic waves are realized by designing phase-encoded metasurfaces. Since then, phase-encoded metasurfaces have become one of the most useful research hotspots [5]. Previously, phase-encoded metasurfaces were divided into two categories: (1) propagation phase designs, which allow the imposition of independent and arbitrary phase profiles on each of the two orthogonal linear polarizations, and (2) geometric or Pancharatnam-Berry (PB) phase designs, which allow imparting equal and opposite phase profiles on two different circular polarizations [6].

Aiming to be miniaturized and highly integrated, multifunctional phase-encoded metasurfaces have attracted tremendous interests and become a research focus. In recent years, several multifunctional phase-encoded metaholograms [7–14], hologram generators [15–17], vortex-encoded information devices [18], and metaprocessor [19] have been proposed. Therein, the propagation phase or PB phase is always used to obtain a linear phase gradient [20]. However, most of them operate in the

*zhulei@qjhr.edu.cn

†sburokur@parisnanterre.fr

‡xuminding@hit.edu.cn

reflection or transmission semispace. For example, Iqbal *et al.* designed a dual-band reflective metahologram that could provide two distinct information channels whose field-intensity distributions can be independently manipulated at the same time [21]. The phase-encoding metasurface can, respectively, present two different letters on dual frequency bands. However, the above scheme is achieved only in a semi-imaging space (reflection space), which limits the potentials of metasurface holograms. As half of the space is not exploited, resources of electromagnetic waves are wasted, and the viewing angle of the metahologram is also limited to half-space imaging. In order to meet the increasing demand for multifunctional electromagnetic equipment and improve the utilization of electromagnetic resources, it is necessary and meaningful to design a monolayer metadevice to realize multichannel metaholograms in the whole space. In 2021, a single-layer transmissive and reflective phase-encoded metasurface was designed by Wu *et al.* [22]. As a result, two independent foci could be obtained in the transmission and reflection spaces of the phase-encoded metasurface for two orthogonal linear-polarized (LP) incident illuminations. Although the reported full-space metahologram is able to achieve dual-channel functionality, it is not conducive to the integration of multifunctional electromagnetic equipment. There is still a lot of capacities for the modulation of electromagnetic waves in transmission and reflection regions simultaneously. Therefore, it is still of great significance to design a high-performance, single-layer, multifunctional (more than two channels) transmission-reflection integrated phase-encoded metasurface.

Here, a quad-channel phase-encoded metasurface is proposed, which is able to tailor electromagnetic wave fronts in full space. The metasurface is composed of two different metal layers printed on the faces of a single dielectric substrate. In accordance with the propagation phase principle, LP waves can be manipulated under reflection mode by changing the structural parameters of the metal patterns. Hence, the phase-encoded metasurface can realize both “*T*” image and “single focus” at $f_1 = 13$ GHz in the reflection semispace. Based on the PB phase principle, the circular-polarized (CP) waves can be tailored by rotating the metal structures on both sides of the dielectric substrate for the transmission mode. The phase-encoded metasurface can then realize, in the transmission semispace, two other different functions of “dual foci” and “four foci” at $f_2 = 10$ GHz and $f_3 = 7.5$ GHz. Depending on the polarization state of the incident illumination, the metasurface operates in transmission region or reflection region. For a proof-of-concept validation, the phase-encoded metasurface platform with electromagnetic imaging functions is designed, fabricated, and measured. The experimental results agree well with the numerical simulation results. The proposed multifunctional phase-encoded metasurface presents advantages in utilizing polarization and space

resources, and has potential applications in multichannel information processing and multifunctional imaging systems.

II. DESIGN OF CODING META-ATOM

Figure 1 shows a schematic illustration of the proposed coding metasurface. It can be expected that a normally incident LP wave will be converted into an *x*-polarized reflected wave or *y*-polarized reflected wave at the frequency of 13 GHz. At the same time, for the normally incident left-handed circular-polarized (LCP) wave, the wave-front control of transmitted waves can be achieved independently at two different frequencies (10 and 7.5 GHz). This not only requires to accurately control the reflection and transmission phases of the unit cell, but also imposes to maintain high reflectivity and high transmittance within the operating frequency band [23]. In addition, the crosstalk between the four working states should be suppressed, since crosstalk directly determines the performance of the metasurface and may deteriorate the independent manipulation of the different working states.

In order to achieve phase modulation of electromagnetic waves in the whole space, the design of the meta-atom is vital and challenging. When LP electromagnetic waves are incident, the reflection and transmission characteristics of the meta-atom (only the co-polarization is considered) can be described as [24]

$$R = \begin{bmatrix} r_{xx} e^{i\phi_x^r} & 0 \\ 0 & r_{yy} e^{i\phi_y^r} \end{bmatrix}, \quad (1)$$

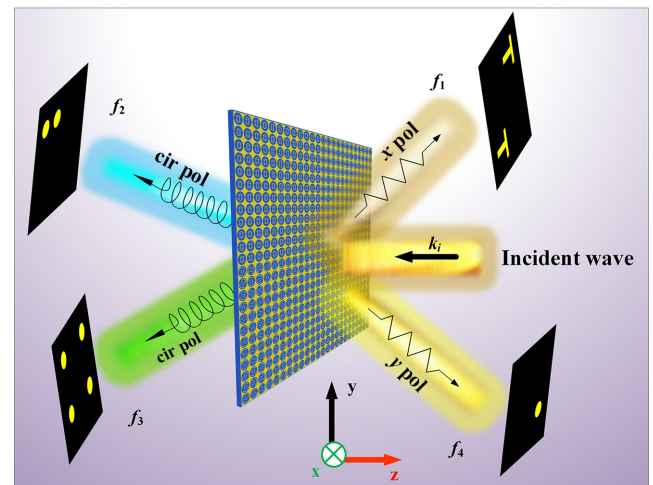


FIG. 1. Schematic illustration of the phase-encoded metasurface.

$$T = \begin{bmatrix} t_{xx}e^{i\varphi_x^t} & 0 \\ 0 & t_{yy}e^{i\varphi_y^t} \end{bmatrix}. \quad (2)$$

r_{xx} , t_{xx} , r_{yy} , and t_{yy} represent the co-polarized reflection and transmission amplitudes under x - and y -polarized wave, respectively. φ_x^r , φ_x^t , φ_y^r , and φ_y^t are the corresponding phase shifts. According to the energy conservation law, $|r_{xx}|^2 + |t_{xx}|^2 = 1$, $|r_{yy}|^2 + |t_{yy}|^2 = 1$. To achieve perfect reflection under the LP state (i.e., $|r_{xx}| = 1$, $|r_{yy}| = 1$) by modulating the structural parameters of the meta-atom, the phase shifts φ_x^r and φ_y^r can be arbitrarily modulated. Under CP incident illuminations, it is expected that the designed meta-atom satisfies a geometric phase condition, which can lead to the transmission and reflection of CP waves with high efficiency. For transmission, a transmission matrix can be represented as follows [25,26]:

$$T = \begin{pmatrix} \cos 2\theta & \sin 2\theta \\ \sin 2\theta & -\cos 2\theta \end{pmatrix}, \quad (3)$$

where θ represents the azimuth rotation angle. Adopting along the $-z$ axis of the meta-atom as the reference direction, the Jones vector can be expressed as

$$E_{in}(r, \theta) = E_o(r, \theta) \begin{pmatrix} 1 \\ \sigma_i \end{pmatrix}, \quad (4)$$

where $E_{in}(r, \theta)$ means the field of an input and $\sigma = \pm 1$. Next, combining Eqs. (3) and (4), the output electric field can be obtained as Eq. (5):

$$E_{out}(r, \varphi) = E_o(r, \varphi) e^{i2\sigma\theta} \begin{pmatrix} 1 \\ -\sigma_i \end{pmatrix}. \quad (5)$$

Here, $\varphi = 2\sigma\pi$. The reflection mode is similar to the transmission mode except that the propagation direction is opposite. Therefore, we manipulate the phase of each element on metasurfaces individually from 0° to 360° by rotating the structure according to the aforementioned geometric phase theory.

Based on the above analysis, a scheme of coding unit cell with high efficiency and high isolation is designed, as shown in Fig. 2. The coding unit cell consists of metal structures (I and II) printed on the faces of a dielectric substrate. The dielectric constant of the substrate is $\epsilon_r = 2.2$, the thickness is $h = 2$ mm, and the loss tangent is $\tan \delta = 0.001$. In the simulations using CST microwave commercial software, periodic boundaries are applied along the x and y axes, and Floquet ports are used along the z axis. Layer I is composed of two double split-ring metal resonators (DSRRs) surrounded by copper, and layer II is formed by a circular patch and a C-shaped metal ring. The opening angles of the DSRRs is $\beta = 45^\circ$ and the C-shaped metal ring is both $\beta_1 = 22.5^\circ$. In structure I shown in Fig. 2, r_1 represents the radius of the hollowed circle. r_2 and r_3 are the outer radius of the large and small split ring of the DSRRs, respectively. w is the width of the split rings, θ_1 is the rotation angle of DSRRs, and β is the opening angle of the splits in the DSRRs. In structure II, r_4 is the inner radius of the C-shaped metal ring and r_5 denotes the radius of the circular metal patch. θ is the rotation angle of the C-shaped metal ring and β_1 is the opening angle of the split in the C-shaped ring. Due to the symmetrical feature of the meta-atom, the characteristics under LCP or RCP (right-handed circular-polarized) incident wave excitation in transmission mode are similar. Crosstalk between different layers (metals I and II) can influence or even destroy the performance of the whole array. Therefore, in our scheme, the characteristics of the unit are studied by changing the dimension of structure I or rotating the angles of structures I and II.

For the reflection mode, according to the principle of propagation phase, the DSRRs in layer I are used to control the reflection phase under LP incident wave. For normally incident x -polarized electromagnetic wave illumination, the amplitude and phase of the meta-atom for the reflection state is shown in Figs. 3(a) and 3(b), when the value of the parameter r_2 is changed. The reflection amplitude of unit cell at 13 GHz is almost unchanged, and the phase difference is almost 180° , which meets the requirement of 1-bit phase encoding. When the y -polarized

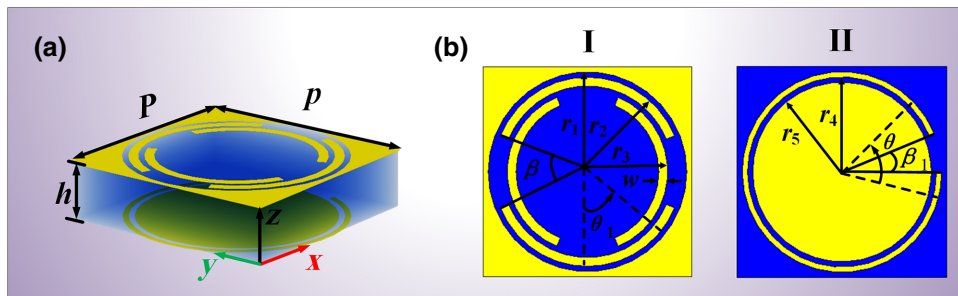


FIG. 2. Schematic diagram of meta-atom. (a) Perspective view of unit structure. (b) Exploded view of unit structure. The geometrical parameters are $p = 12$ mm, $r_1 = 5.7$ mm, $r_4 = 5.4$ mm, $r_5 = 5.1$ mm, $w = 0.5$ mm, and $h = 2$ mm.

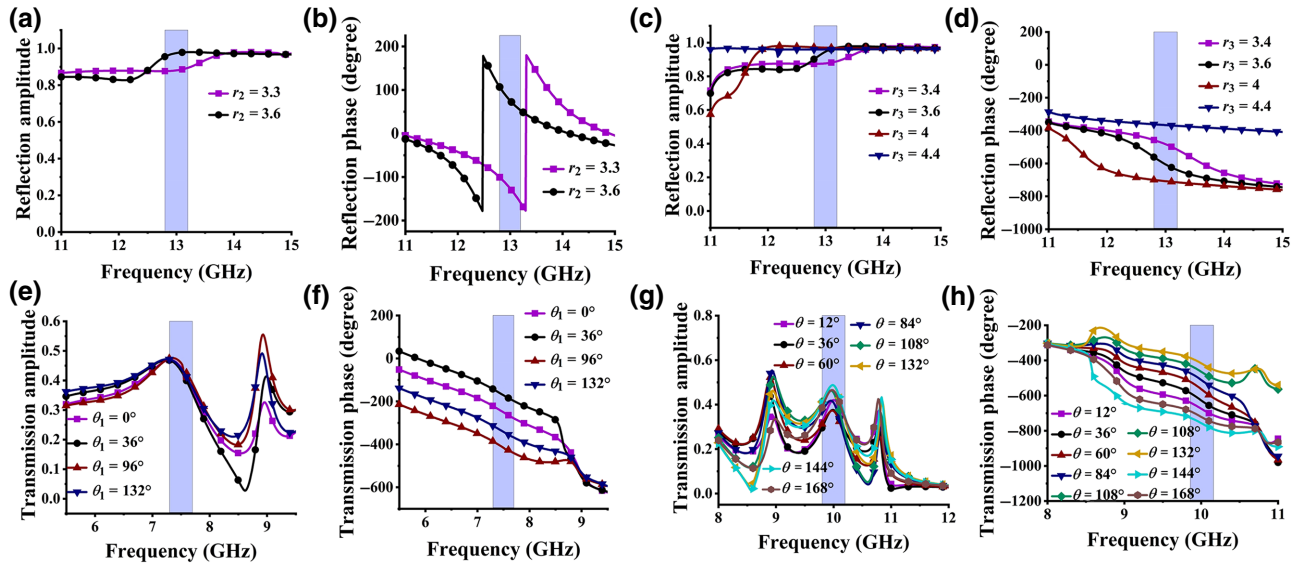


FIG. 3. Characteristics of the meta-atom. (a),(b) Reflection amplitude and phase under x -polarization state at 13 GHz. (c),(d) Reflection amplitude and phase under y -polarization state at 13 GHz. (e),(f) Transmission amplitude and phase under LCP state at 7.5 GHz. (g),(h) Transmission amplitude and phase under LCP state at 10 GHz.

electromagnetic wave illuminates the unit normally, the meta-atom can achieve 2-bit phase encoding at 13 GHz by changing r_3 as shown in Figs. 3(c) and 3(d). The eight coding meta-atoms are extracted during this process, which can be digitally described by Fig. 4. Here, the binary numbers before and after the slash denote the digital code of the meta-atoms under the x - and y -polarized modes, respectively. Meanwhile, the digital states of 0 and 1 stand for reflection phases of 0° and 180° , respectively. And the digital states of 00, 01, 10, and 11 stand for reflection phases of 0° , 90° , 180° , and 270° , respectively.

For the transmission mode, based on the PB phase principle, the unit can realize electromagnetic wave-front manipulation when the rotation angles (θ_1 is the rotation angle of DSRRs and θ is the rotation angle of C-shaped metal ring) are modulated in the transmission space. When the excitation wave is a LCP electromagnetic wave, the phase coverage range of the unit is close to 270° at 7.5 GHz by rotating the angle θ_1 of C-shaped metal ring on the bottom face of the substrate to achieve 2-bit transmission phase encoding. By rotating the angle θ of the DSRRs on the top face of the substrate, 3-bit transmission phase encoding can be realized at 10 GHz. From Figs. 3(e) and 3(f), it can be seen that the transmission amplitude is almost constant (about 0.45) at 7.5 GHz, and the transmission phase difference is almost 270° . Similarly, when θ changes from 60° to 168° , the transmission characteristics of the coding unit are shown in Figs. 3(g) and 3(h). The transmission amplitudes are all around 0.4 at 10 GHz and 360° phase coverage is achieved. The proposed coding unit is then able to achieve 3-bit phase encoding. The 32 coding meta-atoms are extracted during this process,

which can be digitally described by Fig. 5. The binary numbers before and after the slash denote the digital code of the meta-atoms at the lower and higher frequency bands, respectively. Meanwhile, the digital states of 00, 01, 10, and 11 stand for transmission phases of 0° , 90° , 180° , and

x pol		
Digital code	0	1
$r_2 = 3.3 \text{ mm}$	$r_2 = 3.6 \text{ mm}$	
00	$0/00$	$1/00$
$r_3 = 4.4 \text{ mm}$		
01	$0/01$	$1/01$
$r_3 = 3.6 \text{ mm}$		
10	$0/10$	$1/10$
$r_3 = 3.4 \text{ mm}$		
11	$0/11$	$1/11$
$r_3 = 4 \text{ mm}$		

FIG. 4. Detailed structural parameters corresponding to the quad-channel phase-encoded meta-atoms for the reflection mode. The binary numbers before and after the slash denote the digital code of the meta-atoms under the x - and y -polarized mode, respectively.

For LCP @ 10 GHz								
Digital code	000	001	010	011	100	101	110	111
00 $\theta_1 = 36^\circ$	00/000	00/001	00/010	00/011	00/100	00/101	00/110	00/111
01 $\theta_1 = 0^\circ$	01/000	01/001	01/010	01/011	01/100	01/101	01/110	01/111
10 $\theta_1 = 132^\circ$	10/000	10/001	10/010	10/011	10/100	10/101	10/110	10/111
11 $\theta_1 = 96^\circ$	11/000	11/001	11/010	11/011	11/100	11/101	11/110	11/111

FIG. 5. Detailed structural parameters corresponding to the quad-channel phase-encoded meta-atoms for the transmission mode. The binary numbers before and after the slash denote the digital code of the meta-atoms at the lower and higher frequency bands, respectively.

270°, respectively. And the digital states of 000, 001, 010, 011, 100, 101, 110, and 111 stand for transmission phases of 0°, 45°, 90°, 135°, 180°, 225°, 270°, 315°, and 360°, respectively.

Moreover, the study of crosstalk is essential when designing the meta-atom, because it will directly influence

or even destroy the performance of metasurface [26,27]. First, we study the crosstalk on the reflection characteristics of meta-atom for x - and y -polarization states, as shown in Fig. 6. It can be seen from Figs. 6(a), 6(c), and 6(e) that the reflection amplitude and phase of the unit are hardly affected by r_3 , θ_1 , and θ at 13 GHz. For y -polarization state,

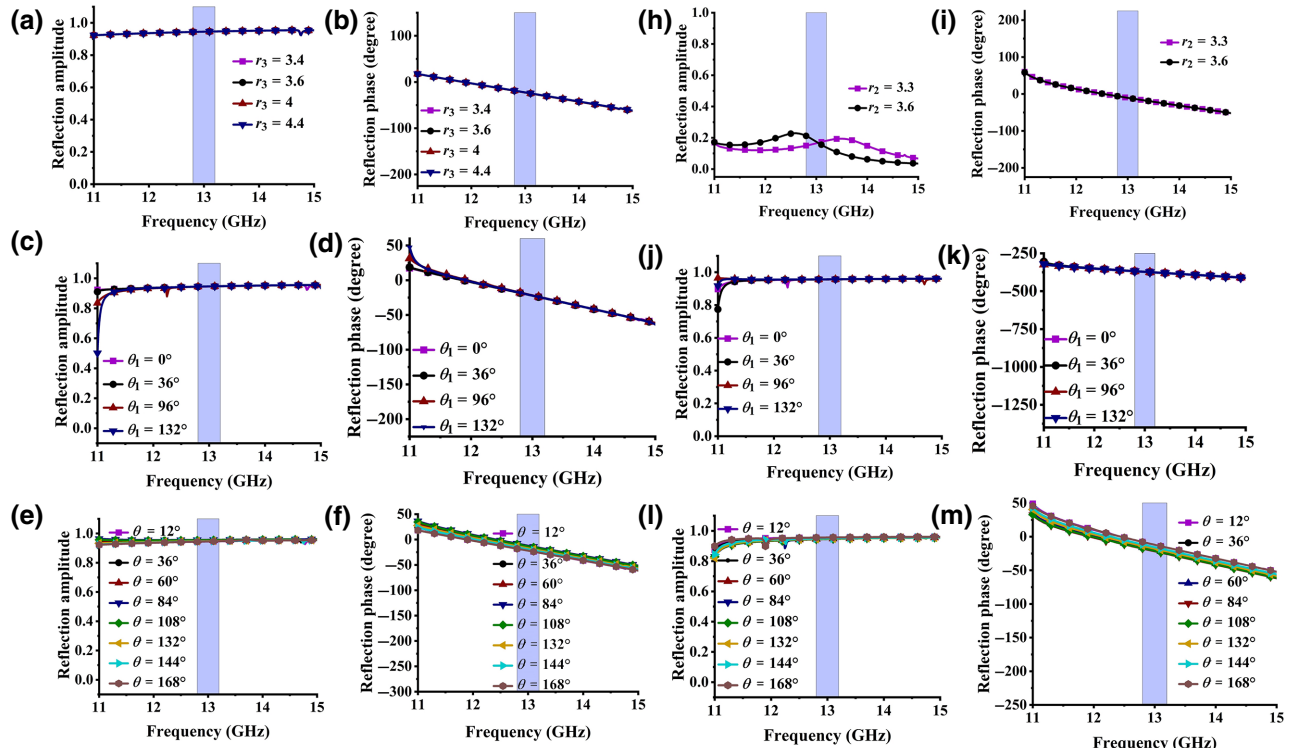


FIG. 6. Crosstalk on the reflection characteristics of meta-atom for x - and y -polarization states. (a),(b) Reflection amplitude and phase when changing r_3 for x -polarization state. (c),(d) Reflection amplitude and phase when modulating θ_1 for x -polarization state. (e),(f) Reflection amplitude and phase when changing θ for x -polarization state. (h),(i) Reflection amplitude and phase when modulating r_3 for y -polarization state. (j),(k) Reflection amplitude and phase when changing θ_1 for y -polarization state. (l),(m) Reflection amplitude and phase when modulating θ for y -polarization state.

the reflection amplitude and reflection phase are also not affected by r_2 , θ_1 , and θ at 13 GHz. Next, the transmission characteristics of the meta-atom are shown in Fig. 7 at 10 and 7.5 GHz for LCP incident state. It is found that the parameters r_2 , r_3 , and θ have no effect on the transmission characteristics (at 7.5 GHz) of the meta-atom when LCP electromagnetic wave is excited. Similarly, modulating r_2 , r_3 , and θ_1 has no effect on the transmission characteristics of the unit at 10 GHz.

In summary, according to the principles of propagation phase and geometric phase, the proposed metasurface not only satisfies the requirements of high amplitude and superior phase modulation in different modes, but also has good isolation properties among the four modes, which provides a good foundation for the independent manipulation of electromagnetic waves.

III. DESIGN OF MULTIFUNCTIONAL METAHOLOGRAM

In order to verify the effectiveness of full-space electromagnetic wave-front regulation, the above-mentioned meta-atoms are arranged in an array according to certain rules to form the phase-encoded metasurface, which contains four different encoding modes and can realize four independent functions at different frequencies. A metahologram composed of 12×12 units is designed by the Gerchberg-Saxton (GS) algorithm [28–30]. The target letter “T” is subjected to Fourier transform and iterative operations are performed to obtain its phase-encoding layout. Then, three other polarization-dependent transmission and reflection focusing phase-encoded distributions are further implemented. They are a single-focus phase-encoded

profile composed of 12×12 coding units, a dual-focus phase-encoded profile composed of 12×12 coding units and a four-focus phase-encoding profile composed of 24×24 coding units.

The phase distribution for focusing obeys the following equation [22]:

$$\varphi(x, y) = \frac{2\pi}{\lambda_0} \left(\sqrt{(x_0 - x)^2 + (y_0 - y)^2 + z_0^2} - |z_0| \right) + \varphi_0, \quad (6)$$

where (x_0, y_0, z_0) represents the coordinates of the design focus, $|z_0|$ is the focal length, φ_0 is the transmission or reflection phase at (x_0, y_0) on the metasurface, and $\varphi(x, y)$ represents the phase at (x, y) . λ_0 represents the working wavelength. Finally, we integrate the above four phase-encoded distributions on a single metasurface platform to form a multifunctional metahologram composed of 24×24 coding units, with a total size of $288 \times 288 \text{ mm}^2$.

To illustrate the four different functions, we set the holographic imaging distance under x -polarized (reflection) incident wave to 10 mm and calculate its phase mask through the GS algorithm, as shown in Fig. 8(a). The focal length under y -polarized (reflection) incident wave is set to $|z_{f_4}| = 100 \text{ mm}$ and the focal lengths under LCP (transmission) incident wave are set to $|z_{f_2}| = 60 \text{ mm}$ and $|z_{f_3}| = 30 \text{ mm}$. The phase distribution of the focusing phase-encoded metasurface is calculated by Eq. (6) under different polarization states, as shown in Figs. 8(b)–8(d).

The model of the phase-encoded metasurface is simulated and the electric field intensity distribution in the xoy plane of the near-field region is extracted under x -polarized, y -polarized, and LCP-polarized waves. The

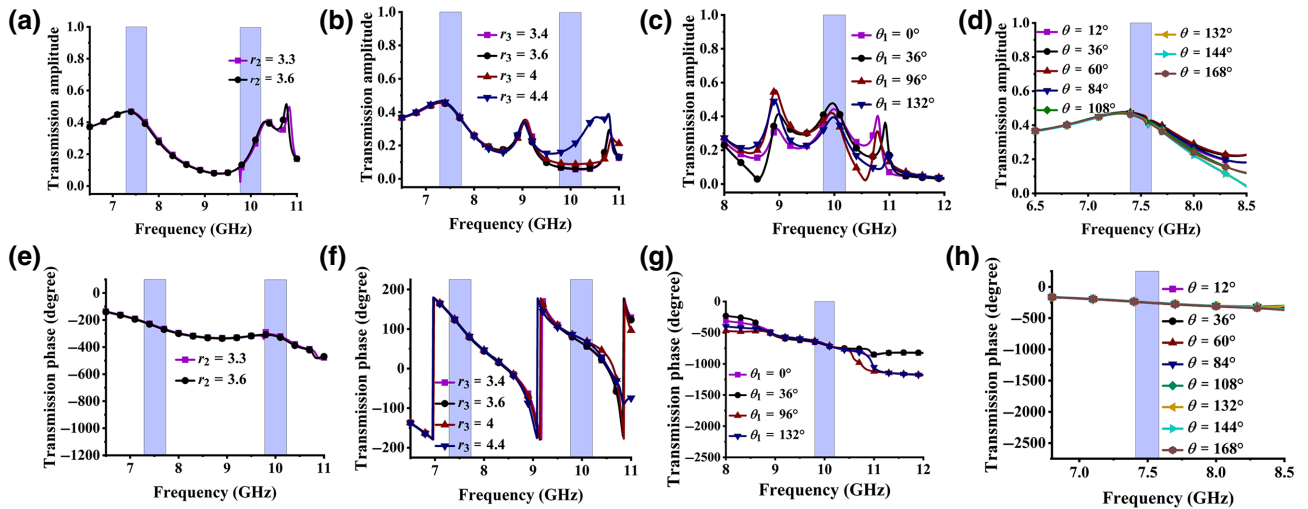


FIG. 7. Crosstalk on the transmission characteristics of meta-atom for LCP state. (a),(b) Transmission amplitude when modulating r_2 and r_3 at 7.5 and 10 GHz, respectively. (e),(f) Transmission phase when modulating r_2 or r_3 at 7.5 and 10 GHz, respectively. (c),(g) Transmission amplitude and phase when modulating θ_1 at 10 GHz. (d),(h) Transmission amplitude and phase when modulating θ at 7.5 GHz.

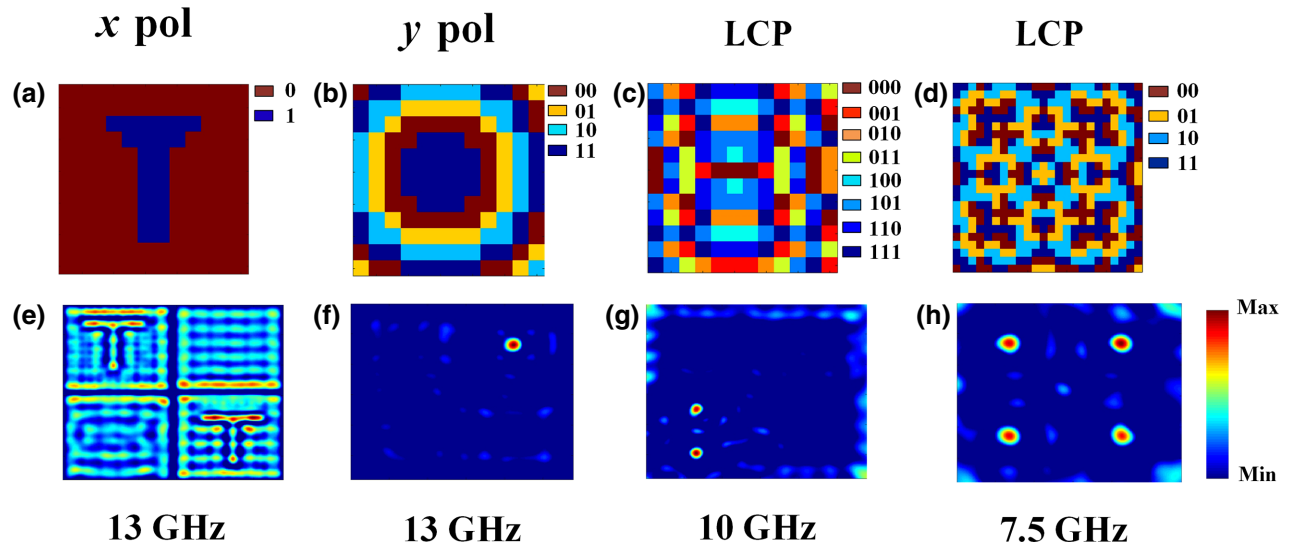


FIG. 8. Phase-encoding layout and simulation results of the quad-functional metahologram. Phase distribution of (a) letter image “*T*”, (b) single focus, (c) dual foci, and (d) quad foci. Simulation results of the metasurface (e) at 13 GHz under *x*-polarized incident wave, (f) at 13 GHz under *y*-polarized incident wave, (g) at 10 GHz under LCP incident wave, and (h) at 7.5 GHz under LCP incident wave.

simulation results are shown in Figs. 8(e)–8(h). Obviously, for the reflection mode, both *x*- and *y*-polarized waves can be reflected by the proposed metasurface at 13 GHz. Here, when excited by *x*-polarized electromagnetic waves, the metasurface reconstructs the letter image “*T*” in the second and fourth quadrants at $z = 10$ mm, as shown in Fig. 8(e). When the *y*-polarized electromagnetic wave illuminates the metasurface, a single-focus image is produced at $z = 100$ mm, as shown in Fig. 8(f). For the transmissive space, when LCP waves illuminate the metasurface, the dual foci are observed at 10 GHz, whose focal plane is $z = -30$ mm, and the quad foci appears at 7.5 GHz in the focal plane $z = -60$ mm. The simulation results show that the reflection efficiencies of “*T*” and “single foci” are 93.2% and 87.9%, respectively, in the reflective channels. For the transmissive channels, the transmission efficiencies of “dual foci” and “four focus” are 40.4% and 42.1%, respectively. Here, the reflection and transmission efficiency refer to the ratio of the output energy to the total incident energy. Besides, the reflection efficiencies are much higher than the transmission ones, which may be since the reflective channels utilize co-polarization wave irradiation, while the cross-polarization wave is adopted in transmissive channels, and some electromagnetic waves are consumed in the CP conversion during PB phase modulation.

IV. EXPERIMENTAL VERIFICATION

To experimentally validate the above features, a sample of the proposed phase-encoded metasurface is fabricated using the conventional printed-circuit-board technique.

Photographs of the top and rear views are shown in Figs. 9(a) and 9(b), respectively. A monolayer double-face copper-cladded metasurface is realized, which has a total size of 288×288 mm². The experimental tests are carried out in a microwave anechoic chamber, and the schematic description of the experimental setup is shown in Fig. 9(c). A 2–18-GHz broadband horn antenna placed at a distance of 20λ is utilized to launch the incident quasi-plane-waves onto the metasurface. The *x*- and *y*-polarized reflected, as well as the LCP-transmitted electric fields in the image planes are measured with an EFS-105-12 fiber-optic active near-field probe, which has a purely dielectric head of 6.6×6.6 mm², allowing negligible field perturbation to be obtained. Both the horn antenna and the probe are connected to an Agilent 8722ES vector network analyzer (VNA). The probe is moved in small increments of 2 mm in *xoy* plane to obtain a full two-dimensional spatial distribution of the electric field.

For the reflection measurement, two steps are required. The first one consists in measuring the incident field without the metasurface sample and the second one consists in measuring the field in the presence of the metasurface, which involves collecting both incident and reflected fields. Then, postprocessing is conducted to extract only the reflected electric field distribution. A scanning surface of 288×288 mm² is used to measure the reflection image, where the probe is placed in the reflection semispace. The reflected hologram images at 13 GHz are measured in the *xoy* plane at 10 mm (for *x*-polarization mode) and 100 mm (for *y*-polarization mode) away from the metasurface, and are displayed in Figs. 9(d) and 9(e), respectively. Finally, the transmitted hologram image at 10 and

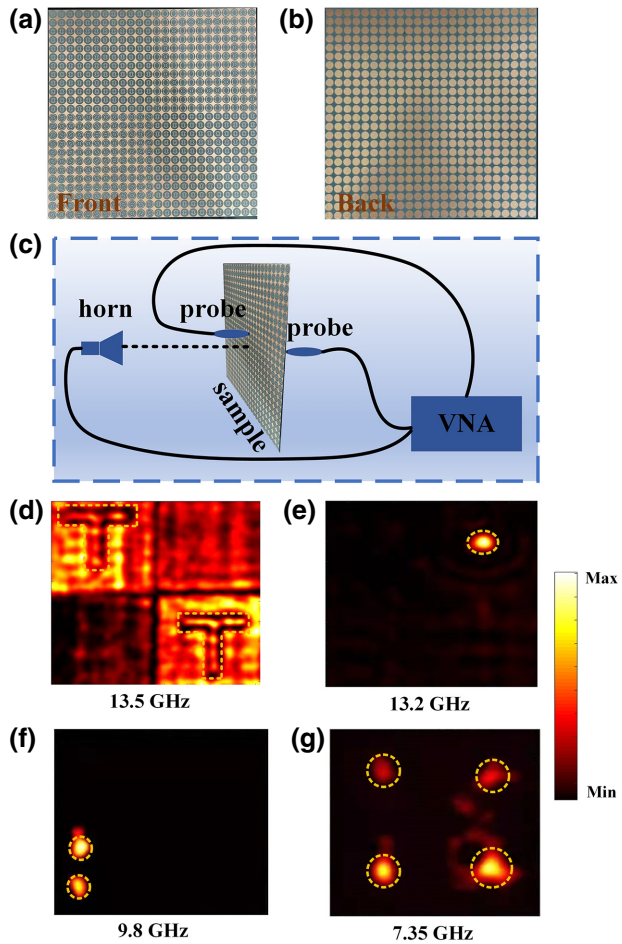


FIG. 9. Experimental results of the quad-functional metahologram. (a),(b) Photograph of the front and rear faces of the metasurface sample. (c) Description of the experimental measurement setup. Experimental images produced by the metahologram (d),(e) in reflection mode, (f),(g) in transmission mode.

7.5 GHz is measured at 30 and 60 mm away from the metasurface, respectively, and the images are shown in Figs. 9(f) and 9(g). In order to measure the transmission image, the near-field probe is placed in the transmission semispace, as shown in Fig. 9(c).

As it can be clearly observed, for x -polarization mode, the simulation [Fig. 8(e)] and measurement [Fig. 9(d)] results show that the image quality is not very good and the background noise is slightly serious. This phenomenon can be due to the diffraction efficiency as well as to the phase quantization level [31,32]. The two-level quantization of this reflection channel undoubtedly limits the imaging quality. Therefore, the image quality and diffraction efficiency can be both optimized by increasing the phase quantization level, but this improvement is limited. When higher phase quantization level is used, the background noise will be reduced especially for complex holographic images [32]. Moreover, the low imaging quality may be

due to the limited size of the metasurface prototype. For LCP mode, the imaging quality in the experimental results at 7.35 GHz is found to be a little bad, which may be due to the unequal amplitude of the coding unit cell and the limited size of the metasurface sample. The quantization level of phase is also a key factor affecting the efficiency. The imaging quality can be improved by adopting a 3-bit phase-encoding scheme, but the cost of possible higher design complexity. Due to the finite size of the metasurface, the proposed metahologram is inevitably affected by other modes when working in the transmission mode. In addition, the operating frequencies in experiments show a slight frequency shift, which may be caused by the fabrication tolerances. However, the experimental results are basically consistent with the simulation results.

V. CONCLUSION

The designed four-channel coding metasurface can be used for holograms, which can produce different images in transmission and reflection spaces. The proposed meta-atoms are composed of judiciously designed structures with polarization-dependent properties based on double-face copper-cladded patterns on a single-layer substrate, to efficiently regulate the phase of EM waves in four information channels. Moreover, the proposed concept can also be implemented with dynamic manipulation capabilities by exploiting judiciously designed meta-atoms and tunable mechanisms such as nematic liquid crystals [33], lumped electronic components [34], and micromotors [35] to change the reflection and transmission responses. In addition to the above four functions, other coding modes can be selected to verify such a multifunctional device. Compared with previously reported schemes [22,34,35], the proposed metasurface has well-developed multifunctional characteristics, which can realize independent control of four channels simultaneously at different frequencies in the transmission and reflection spaces. In addition, the proposed metasurface presents the advantages of displaying a simple structure and easy fabrication processing since it involves a single dielectric substrate layer. So, the proposed design is conducive to system integration and equipment miniaturization, and can be used as high-efficiency electromagnetic equipment [36], polarization beam splitter [37], and radomes [37,38]. In summary, as long as the corresponding coding mode is carefully designed, the proposed phase-encoding metasurface can realize any four independent functions.

ACKNOWLEDGMENTS

This paper is supported by the Scientific and technological development project of the central government guiding local (SBZY2021E076), Postdoctoral Research Fund Project of Heilongjiang Province of China (LBH-Q21195), Fundamental Research Funds of Heilongjiang

Provincial Universities of China (135509227), Natural Science Foundation of Heilongjiang Province (LH2022F053), and National Natural Science Foundation of China (NSFC) (61501275).

DATA AVAILABILITY

The data that support the findings of this study are available from the corresponding author upon reasonable request.

- [1] D. Gabor, A new microscopic principle, *Nature* **161**, 777 (1948).
- [2] X. Li, H. Hou, K. Liu, J. Lou, G. Wang, and T. Cai, Circularly polarized transmissive meta-holograms with high fidelity, *Adv. Photonics Res.* **2**, 2100076 (2021).
- [3] G. Lee, G. Yoon, S. Lee, H. Yun, J. Cho, K. Lee, H. Kim, J. Rho, and B. Lee, *Nanoscale* **10**, 4237 (2018).
- [4] A. Buff, A. A. Serra, P. Nepa, H. T. Chou, and G. Manara, A focused planar microstrip array for 2.4 GHz RFID readers, *IEEE Trans. Antennas Propag.* **58**, 1536 (2010).
- [5] X. Yang, J. Luo, H. Chen, H. Xiao, Z. Zhu, J. Chen, K. Huang, and J. Yuan, Analysis and design of a multi-function metasurface, *Mater. Res. Exp.* **6**, 045801 (2019).
- [6] J. P. Balthasar Mueller, N. A. Rubin, R. C. Devlin, B. Groever, and F. Capasso, *Phys. Rev. Lett.* **118**, 113901 (2017).
- [7] Y. H. Guo, M. B. Pu, Z. Y. Zhao, Y. Q. Wang, and X. G. Luo, Merging geometric phase and plasmon retardation phase in continuously shaped metasurfaces for arbitrary orbital angular momentum generation, *ACS Photonics* **3**, 2022 (2016).
- [8] F. Zhang, M. B. Pu, X. Li, P. Cao, X. L. Ma, and X. G. Luo, All-dielectric metasurfaces for simultaneous giant circular asymmetric transmission and wavefront shaping based on asymmetric photonic spin-orbit interactions, *Adv. Funct. Mater.* **27**, 1704295 (2017).
- [9] L. Li, H. Ruan, C. Liu, Y. Li, Y. Shuang, A. Alù, C. W. Qiu, and T. J. Cui, Machine-learning reprogrammable metasurface imager, *Nat. Commun.* **10**, 1082 (2019).
- [10] L. Zhang, R. Y. Wu, G. D. Bai, H. T. Wu, Q. Ma, X. Q. Chen, and T. J. Cui, Transmission-reflection-integrated multifunctional coding metasurface for full-space controls of electromagnetic waves, *Adv. Funct. Mater.* **28**, 1802205 (2018).
- [11] Y. B. Zhang, H. Liu, H. Cheng, J. G. Tian, and S. Q. Chen, Multidimensional manipulation of wave fields based on artificial microstructures, *Opto-Electron. Adv.* **3**, 200002 (2020).
- [12] K. Chen, N. Zhang, G. W. Ding, J. M. Zhao, T. Jiang, and Y. J. Feng, Active anisotropic coding metasurface with independent real-time reconfigurability for dual polarized waves, *Adv. Mater. Technol.* **5**, 1900930 (2020).
- [13] N. Zhang, K. Chen, Y. Zheng, Q. Hu, K. Qu, J. Zhao, J. Wang, and Y. Feng, Programmable coding metasurface for dual-band independent real-time beam control, *IEEE J. Emerg. Sel. Topics Circuits Syst.* **10**, 20 (2020).
- [14] R. Y. Wu, L. Zhang, L. Bao, L. W. Wu, Q. Ma, G. D. Bai, H. T. Wu, and T. J. Cui, Digital metasurface with phase code and reflection-transmission amplitude code for flexible full-space electromagnetic manipulations, *Adv. Opt. Mater.* **7**, 1801429 (2019).
- [15] X. Ding, Z. Wang, G. Hu, J. Liu, K. Zhang, H. Li, B. Ratni, S. Burokur, Q. Wu, J. Tan, and C. Qiu, Metasurface holographic image projection based on mathematical properties of Fourier transform, *Photonix* **1**, 16 (2020).
- [16] Z. Zhao, Y. Wang, C. Guan, K. Zhang, Q. Wu, H. Li, J. Liu, S. Burokur, and X. Ding, Deep learning-enabled compact optical trigonometric operator with metasurface, *Photonix* **3**, 15 (2022).
- [17] J. Ni, S. Liu, G. Hu, Y. Hu, Z. Lao, J. Li, Q. Zhang, D. Wu, S. Dong, J. Chu, and C. Qiu, Giant helical dichroism of single chiral nanostructures with photonic orbital angular momentum, *ACS Nano* **15**, 2893 (2021).
- [18] L. Jin, Y. Huang, Z. Jin, R. Devlin, Z. Dong, S. Mei, M. Jiang, W. Chen, Z. Wei, H. Liu, *et al.*, Dielectric multi-momentum meta-transformer in the visible, *Nat. Commun.* **10**, 4789 (2019).
- [19] Z. Wang, G. Hu, X. Wang, X. Ding, K. Zhang, H. Li, S. Burokur, Q. Wu, J. Liu, J. Tan, and C. Qiu, Single-layer spatial analog meta-processor for imaging processing, *Nat. Commun.* **13**, 2188 (2022).
- [20] K. Zhang, Y. Yuan, X. Ding, H. Li, B. Ratni, Q. Wu, J. Liu, S. N. Burokur, and J. Tan, Polarization-engineered non-interleaved metasurface for integer and fractional orbital angular momentum multiplexing, *Laser Photonics Rev.* **15**, 2000351 (2021).
- [21] S. Iqbal, H. Rajabalipanaha, L. Zhang, X. Qiang, A. Abdolali, and T. Cui, Frequency-multiplexed pure-phase microwave meta-holograms using bi-spectral 2-bit coding metasurfaces, *Nanophotonics* **9**, 703 (2020).
- [22] J. Wu, Y. Pan, and S. Zheng, Design of single-layer polarization-dependent transmissive and reflective focusing metasurface, *IEEE Trans. Antennas Propag.* **69**, 7637 (2021).
- [23] R. Mao, G. Wang, T. Cai, K. Liu, D. Wang, and B. Wu, Ultra-thin and high-efficiency full-space Pancharatnam-Berry metasurface, *Opt. Exp.* **28**, 31216 (2020).
- [24] H. Yang, Z. Xie, Z. Zhou, and X. Yuan, Full-space polarization-regulated lightwave steering via single-layer metasurfaces, *J. Phys. D: Appl. Phys.* **54**, 015102 (2021).
- [25] M. Akram, G. Ding, K. Chen, Y. Feng, and W. Zhu, Ultra-thin single layer metasurfaces with ultra-wideband operation for both transmission and reflection, *Adv. Mater.* **32**, 1907308 (2020).
- [26] C. Zhang, G. Wang, H. Xu, X. Zhang, and H. Li, Helicity-dependent multifunctional metasurfaces for full-space wave control, *Adv. Opt. Mater.* **8**, 1901719 (2020).
- [27] J. Yang, X. Wu, J. Song, C. Huang, Y. Huang, and X. Luo, Cascaded metasurface for simultaneous control of transmission and reflection, *Opt. Exp.* **27**, 9061 (2019).
- [28] R. W. Gerchberg and W. O. Saxton, A practical algorithm for the determination of phase from image and diffraction plane pictures, *Optik* **35**, 237 (1972).
- [29] J. R. Fienup, Iterative method applied to image reconstruction and to computer-generated holograms, *Opt. Eng.* **19**, 297 (1980).

- [30] X. Jiang, J. Ye, J. He, X. Wang, D. Hu, S. Feng, Q. Kan, and Y. Zhang, An ultrathin terahertz lens with axial long focal depth based on metasurfaces, *Opt. Exp.* **21**, 30030 (2013).
- [31] X. J. Ni, A. V. Kildishev, and V. M. Shalaev, Metasurface holograms for visible light, *Nat. Commun.* **4**, 2807 (2013).
- [32] R. Fu, X. Shan, L. Deng, Q. Dai, Z. Guan, Z. Li, and G. Zheng, Multiplexing meta-hologram with separate control of amplitude and phase, *Opt. Exp.* **29**, 27696 (2021).
- [33] Z. Wang, X. Ding, K. Zhang, B. Ratni, S. Burokur, X. Gu, and Q. Wu, Huygens metasurface holograms with the modulation of focal energy distribution, *Adv. Opt. Mater.* **6**, 1800121 (2018).
- [34] R. Feng, B. Ratni, J. Yi, H. Zhang, A. Lustrac, and S. Burokur, Versatile metasurface platform for electromagnetic wave tailoring, *Photonics Res.* **9**, 09001650 (2021).
- [35] W. Yang, K. Chen, Y. Zheng, W. Zhao, Q. Hu, K. Qu, T. Jiang, J. Zhao, and Y. Feng, Angular-adaptive reconfigurable spin-locked metasurface retroreflector, *Adv. Sci.* **8**, 2100885 (2021).
- [36] Y. Wang, Y. Ge, Z. Chen, X. Liu, J. Pu, K. Liu, H. Chen, and Y. Hao, Broadband high-efficiency ultrathin metasurfaces with simultaneous independent control of transmission and reflection amplitudes and phases, *IEEE Trans. Microwave Theory Tech.* **70**, 254 (2022).
- [37] G. Shang, Z. Wang, H. Li, K. Zhang, Q. Wu, S. N. Burokur, and X. Ding, Metasurface holography in the microwave regime, *Photonics* **8**, 135 (2021).
- [38] Y. Pan, F. Lan, Y. Zhang, G. He, L. Wang, and Z. Yang, Dual-band trifunctional coding metasurfaces based on independent control of transmission and reflection, *Photonics Res.* **10**, 416 (2022).